

# Reactive sputtering of $\text{CS}_x$ thin solid films using $\text{CS}_2$ as precursor

Hans Högberg<sup>a</sup>, Chung-Chuan Lai<sup>a,1</sup>, Esteban Broitman<sup>a,2</sup>, Ivan G. Ivanov<sup>b</sup>, Cecilia Goyenola<sup>a</sup>, Lars-Åke Näslund<sup>a</sup>, Susann Schmidt<sup>a,3</sup>, Lars Hultman<sup>a</sup>, Johanna Rosen<sup>a</sup>, Gueorgui K. Gueorguiev<sup>a,\*</sup>

<sup>a</sup> Thin Film Physics Division, Department of Physics, Chemistry and Biology (IFM), Linköping University, SE-581 83, Linköping, Sweden

<sup>b</sup> Semiconductor Materials Division, Department of Physics Chemistry and Biology (IFM), Linköping University, SE-581 83, Linköping, Sweden

## ARTICLE INFO

### Keywords:

Carbon-based nanostructured materials  
Protective and hard coatings  
Reactive direct current magnetron sputtering  
Thin film characterization

## ABSTRACT

We deposit  $\text{CS}_x$  thin solid films by reactive direct current magnetron sputtering of a C target in an argon plasma, using carbon disulfide ( $\text{CS}_2$ ) as a precursor to film growth. We investigate the influence of the partial pressure of the  $\text{CS}_2$  vapor introduced into the plasma on the composition, the chemical bonding structure, the structural, and the mechanical properties as determined by x-ray photoelectron spectroscopy (XPS), Raman spectroscopy, scanning electron microscopy (SEM), and nanoindentation for films deposited at 150 and 300 °C. The Raman and the XPS results indicate that S atoms are incorporated in mostly  $\text{sp}^2$  bonded C network. These results agree with previous *ab-initio* theoretical findings obtained by modeling of the  $\text{CS}_x$  compound by the Synthetic Growth Concept. The microstructure of the films as well as the results of their Raman characterization and the nano-mechanical testing results all point out that with the increasing S content some  $\text{sp}^3$  bonding is admixed in the predominantly  $\text{sp}^2$  bonded  $\text{CS}_x$  network, leading to typical amorphous structure with short and interlocked graphene-like planes for S contents between 2% and 8%. We conclude that  $\text{CS}_x$  thin solid films deposited by using  $\text{CS}_2$  as a precursor would be  $\text{CS}_x$  films deposited at low temperature of ~150 °C and with an S content in the region of 6 at.% may be interesting candidates for applications as hard/elastic protective coatings.

## 1. Introduction

In the context of reactively sputtered carbon-based thin films containing p-elements, the C–N system was the first to be systematically studied. The initial intention was to reactively sputter C–N thin film in order to achieve the theoretically predicted super hard carbon nitride phase  $\beta\text{-C}_3\text{N}_4$  [1]. However, growth of stoichiometric  $\text{C}_3\text{N}_4$  films was not possible by this technique that instead yielded films with much less nitrogen content than nominal for  $\text{C}_3\text{N}_4$ , usually ~30 at.% and below [2]. The deposited films, today known as fullerene-like (FL) carbon nitride ( $\text{CN}_x$ ) [3], became the first example of what later became a new class of inherently nanostructured thin films that demonstrate technologically relevant properties such as resiliency, hardness, and a relatively low friction coefficient [4]. The properties of FL- $\text{CN}_x$  are attractive in applications such as protective coatings or as solid lubricant. Thus, today C films incorporating N are used to protect hard drives [2]. The promising

results obtained from the FL- $\text{CN}_x$  films initiated both theoretical calculations and experimental work with new deposition techniques on this materials system as well as exploration of new potential FL systems. The concept of incorporating a p-element in a C-based film generates numerous plausible combinations out of a total number of 22 p-elements in the periodic chart, excluding C, the noble gases, and radioactive elements. For instance, looking to the right of N in the 2nd period, we find O and F as potential elements for incorporation in a C-film matrix. Both these elements exhibit higher electronegativity values and valence electron concentrations (VEC) compared to N, which will yield a different type of bonding that might result in new film properties and a new microstructural short-range order (SRO). Carbon fluoride ( $\text{CF}_x$ ) thin films synthesized by reactive high-power impulse magnetron sputtering (HiPIMS) in  $\text{CF}_4$  and  $\text{C}_4\text{F}_8$  have been studied [5,6] and theoretical calculations to predict their formation have been performed [7,8], whereas the strong driving force of O to form gaseous compounds together with C

\* Corresponding author.

E-mail address: [gueorgui.kostov.gueorguiev@liu.se](mailto:gueorgui.kostov.gueorguiev@liu.se) (G.K. Gueorguiev).

<sup>1</sup> Present address: European Spallation Source ERIC, P.O. Box 176, SE-221 00, Lund, Sweden.

<sup>2</sup> Present address: SKF Research and Development Center, 3992AE Houten, Netherlands.

<sup>3</sup> Present address: IHI Ionbond AG, Industriestrasse 211, Olten CH-4600, Switzerland.

has rendered the C–O system less interesting. Depending on the reactive gas flow,  $\text{CF}_x$  thin films with F contents ranging between 2 at.% and 36 at.% have been synthesized [6,8]. Upon F incorporation the microstructure and the mechanical properties of C-based films changed significantly; biocompatible  $\text{CF}_x$  thin films and improved mechanical properties are obtained when the F content is kept below  $\sim 25$  at.%. F contents above 25 at.% yield a soft, polymer-like structure with a super-hydrophobic surface [5,6,9,10]. A limitation for both FL- $\text{CF}_x$  films as well as FL- $\text{CN}_x$  is that they display poor adhesion to substrates of technological importance such as Si(100) and stainless steel [11,12].

To further improve the prospects for applications of any carbon based coatings in general, and of the FL thin films in particular, their diversification by developing new deposition methods, adopting new precursors, and introducing new dopant elements in the C network is necessary. Thus, opportunities for atomic rearrangements, enriched diversity of bonding environments and interplay between  $\text{sp}^2$  and  $\text{sp}^3$  hybridizations are created. Phosphorus (P) is the next period neighbor to N and shows increased options for bonding compared to N seen from point of view of possible d-orbital contribution. This is supported by magnetron sputtering from C–P compound targets, showing that phosphorus carbide ( $\text{CP}_x$ ) thin films exhibit elements of short-range ordering in the form of curved and strongly inter-locked graphene planes with FL structural characteristics [13]. Selected area diffraction (SAED) patterns identified these  $\text{CP}_x$  thin films as different from any other C allotropes, including structures as those in FL- $\text{CN}_x$  [13].

Following our tradition and aiming to enlarge the family of FL compounds, and broadly speaking, those compounds with amorphous structure exhibiting recognizable close order bonding pattern, we choose to investigate the right-side neighbor to P in the Periodic Table that is sulfur (S). Compared to P, S which is to the immediate right of P in the third period of the Periodic Table, shows increased VEC and also more readily available d-orbitals resulting from the higher electronegativity of S atoms. Besides that S-based compounds are known for their low-friction characteristics, it should also be mentioned that S is attractive as a dopant in C systems in order to tune electrical properties such as electron field emission [14] and even superconductivity [15,16]. Recently, S-doped, as well as S/N co-doped graphene-like carbon sheets [17] and S-doped and S/P co-doped porous C-based material for supercapacitor and catalytic applications [18] have been suggested.

Remaining with the class of the FL compounds, it is also of practical interest to study the growth and the properties of selected ternary compounds, thus combining the effects of both hetero elements on the C matrix to possibly achieve a more valuable mix of mechanical and electric properties. In the specific case when the hetero elements are S and F an increased electron mobility, but also an enhanced chemical inertness of the compound, may be expected. The differences in the atomic radius and in the electronic structure between the heteroatoms (in this case S and F) also affect the microstructure and, thus, the mechanical properties of the material. The ternary systems, therefore, provide an extra parameter to tune the properties of the carbon-based thin films compared to the binary systems.

Recently, we have studied the growth of the ternary carbon-based  $\text{CS}_x\text{F}_y$  thin films by using  $\text{SF}_6$  as reactive gas [19]. The properties of the films were characterized and explained in the terms of the interaction of the theoretically predicted C–S–F reactant species that play role during the structure formation of  $\text{CS}_x\text{F}_y$  thin films. The mechanical compliance values indicated that most of the  $\text{CS}_x\text{F}_y$  thin films are highly elastic, and especially the  $\text{CS}_x\text{F}_y$  thin films with low heteroatom content ( $\text{F} + \text{S}$ ) exhibit superelastic behavior, which is a well-known characteristic of carbon thin films with the FL structure. The changes in micro- and nanostructure, and consequently the properties, indicate a strong dependence of the  $\text{CS}_x\text{F}_y$  thin film formation on the  $\text{SF}_6$  partial pressure and the dissociation of its molecule during the growth process [19].

Also, in previous works, we focused on the binary  $\text{CS}_x$  films looking in detail on the structural and energetic implications of introducing S atoms in graphene-like networks from a theoretical point of view by

means of the density functional theory (DFT) based Synthetic Growth Concept [20,21] by sampling sets of competing C and S atomic and molecular species. We showed that odd-member ring defects are stable in  $\text{CS}_x$  model systems [22]. These types of rings are one of the main structural characteristics in FL compounds as they promote curvature in honeycomb networks [3]. Moreover, similarly to N and P, S atoms can form single bonds with three adjacent C atoms to occupy the place of a C atom in graphene-like networks. In contrast to N that sits on an in-plane position [20], the S atoms stick out of the plane inducing local curvature [22]. P shows a similar behavior in  $\text{CP}_x$  model systems [21]. The structural characteristics described and found for the  $\text{CS}_x$  model systems make these systems to a lesser extent FL and more tending to amorphous compound with short and interlocked graphene-like planes. The main conclusion following these results is that  $\text{CS}_x$  thin films with amorphous structure and close order bonding pattern could be expected for S concentrations between 10 and 15 at.% [23]. For this range of S concentrations, the occurrence of defects is enough to obtain smooth and sufficient curvature in the C planes without disrupting the network. In terms of structure,  $\text{CS}_x$  is expected to be intermediate between  $\text{CN}_x$  and  $\text{CP}_x$ , exhibiting enhanced curvature and more cross-linking sites than  $\text{CN}_x$ , but less than  $\text{CP}_x$ . Thus, the aforementioned results show a high potential for  $\text{CS}_x$  as new thin film material, which makes the system interesting to synthesize.

In this study, we deposit  $\text{CS}_x$  thin solid films by reactive direct current magnetron sputtering (rDCMS) of a C target in an argon (Ar) plasma, using carbon disulfide ( $\text{CS}_2$ ) as S precursor as well as for additional C supply to the films. We investigate the influence of the partial pressure of the  $\text{CS}_2$  vapor ( $p\text{CS}_2$ ) introduced into the plasma on the composition, the chemical bonding structure, the structural, and the mechanical properties as determined by x-ray photoelectron spectroscopy (XPS), scanning electron microscopy (SEM), and nanoindentation for films deposited at 150 and 300 °C. Raman spectra were also recorded for all films. We compare our results to previously obtained theoretical and experimental findings.

## 2. Experimental details

The  $\text{CS}_x$  thin solid films were reactively sputtered on  $1 \times 1$  cm Si(100) substrates by rDCMS of a C target in an Ar plasma, using carbon disulfide ( $\text{CS}_2$ ) as a precursor, using a high vacuum system operating at a base pressure of  $\sim 6.7 \times 10^{-5}$  Pa that was previously described in Ref. [13]. The  $\text{CS}_2$  partial pressure was measured before the discharge was ignited. The measurement was conducted by leaking in the precursor and measuring the pressure. In the deposition chamber the target was positioned under the substrate holder, facing the Si(100) substrates along the surface normal, and at a target-to-substrate distance of 7 cm. The  $\text{CS}_2$  was fed into the deposition chamber through a gas-handling system consisting of an evaporator to store the liquid solvent held at room temperature (corresponding vapor pressure at 20 °C of  $\sim 40$  kPa), a needle-valve to regulate the partial pressure of the vapor reaching the plasma, and terminating with a gas pipe inside the chamber to distribute the  $\text{CS}_2$  vapor close to the substrate. All depositions were carried at a sputtering power of 90 W applied to the circular 2-inch C target, a fixed Ar pressure of 0.8 Pa, a substrate bias of  $-25$  V, and with a deposition time of 180 min. This resulted in film thicknesses of  $\sim 530$ – $\sim 660$  nm, corresponding to a deposition rate of  $\sim 3.7$  nm/min for the thickest film. The influence of the  $\text{CS}_2$  partial pressure on the film properties was investigated for substrate temperatures of 150 °C and 300 °C, using  $p\text{CS}_2$  of 0, 2, 3, 4, 8, 16, and 32 mPa for both temperatures and additional  $p\text{CS}_2$  of 64, 100, and 200 mPa for the highest temperature, as monitored by a capacitance manometer. It should be noted that the  $p\text{CS}_2$  of 200 mPa is uncertain because of the applied pressure gauge at these pressures.

Qualitative and quantitative analysis of the films as well as their chemical bonding structure were determined through XPS, using an AXIS Ultra DLD instrument from Kratos Analytical operated at a base

pressure of  $1.5 \times 10^{-7}$  Pa. Survey spectra and S 2p, S 2s, C 1s, and O 1s core-level spectra were recorded with excitation from monochromatic Al K $\alpha$  radiation ( $h\nu = 1486.6$  eV), operating the x-ray anode at 225 W. As the samples were conductors, no charge compensation from low energy electrons was needed. In addition, no sputter-cleaning of the samples was conducted to avoid sputter damages of potential amorphous materials but with close order bonding pattern. It should be noted that the samples were exposed to air for a few minutes while they were transferred between the deposition system and the XPS system. For quantitative analysis, we used the S 2p peak to determine the S content in the films as this peak has the highest intensity, i.e. has the highest photoelectric cross section. The binding energy scale was calibrated by setting the position of the Fermi edge of a sputter-cleaned Ag sample to 0.0 eV [24], which resulted in a position for the Ag 3d $_{5/2}$  core-level peak of 368.30 eV [25]. The film thicknesses and cross-sectional morphology were assessed by SEM from a LEO 1550-FEG instrument that was operated at an acceleration voltage of 5 kV. The cross-sectional SEM samples were prepared by mechanical cleaving of Si substrates.

The Raman spectra were measured using a home-built micro-Raman setup with 100 $\times$  microscope objective (NA = 0.95) and a 532-nm excitation from a solid state laser. The laser power was kept at  $\sim 0.5$  mW at the objective in order to avoid overheating of the sample within the laser spot of diameter  $\sim 0.8$   $\mu$ m. The spectra were detected using a spectrometer (Jobin Yvon, model HR460) with grating of 600 grooves/mm coupled to a CCD camera, resulting in resolution of  $\sim 5.5$  cm $^{-1}$ .

Nanomechanical properties of the films were evaluated by quasi-static displacement-controlled nanoindentation tests using a TI950 Triboindenter (Hysitron). Hardness (H) and reduced elastic modulus ( $E_r$ ), measured with a Berkovich diamond probe of  $\sim 150$  nm tip radius, were calculated according to the classical method proposed by Oliver and Pharr [26]. The tip function area at low penetration depths was carefully calibrated using a fused silica sample. The thermal drift was compensated for before each measurement. Moreover, no pile-up correction was necessary in the softer samples as all nanoindentation impressions have shown a sink-in behavior. In all tests, a total of 12 indents with spacing of  $\sim 10$   $\mu$ m were averaged to determine the mean value and standard deviations of H and  $E_r$ .

When the nanoindenter tip penetrates the surface of a film deposited onto a substrate, the mechanical response of the film will be influenced by the deformation of the substrate. It has been shown that the 10% “rule of thumb”, which states that the indenter should not penetrate more than 10% of the total film thickness, is not always valid [27]. In our experiments, the maximum penetration depth was calculated following the graphical method explained in the ISO 14577 Standard Part 4 [28]. Numerous indentations were done in selected samples at different penetration depths ( $h_{\max}$ ), as shown in Fig. 1. It was observed that at the beginning, the measured hardnesses at low penetration depths are low due to indentation size effects [27]. At deeper penetrations, the hardness increases until it arrives to a maximum value (a plateau) that in our samples occurs at around  $h_{\max} = 50$  nm, and then the value decreases (or increases again) due to the influence of the substrate. The ISO Standard states that this maximum value is the nanoindentation hardness H of the film. From these results, it was concluded that the displacement-controlled nanoindentation experiments should be carried out in our samples at  $h_{\max} = 50$  nm indentation depth.

### 3. Results and discussion

#### 3.1. Composition analysis of the CS $_x$ films

Table 1 summarizes all CS $_x$  film samples (L1 - L9 deposited at 150 °C, and H1 - H11 deposited at 300 °C), together with the corresponding deposition pressure of CS $_2$  and their composition assessed by XPS. Fig. 2 shows the S content for films deposited at 150 and 300 °C, using different pCS $_2$  in the plasma. As seen from Fig. 2, the S content increases with the increasing CS $_2$  content in the plasma. The inset in Fig. 2 shows

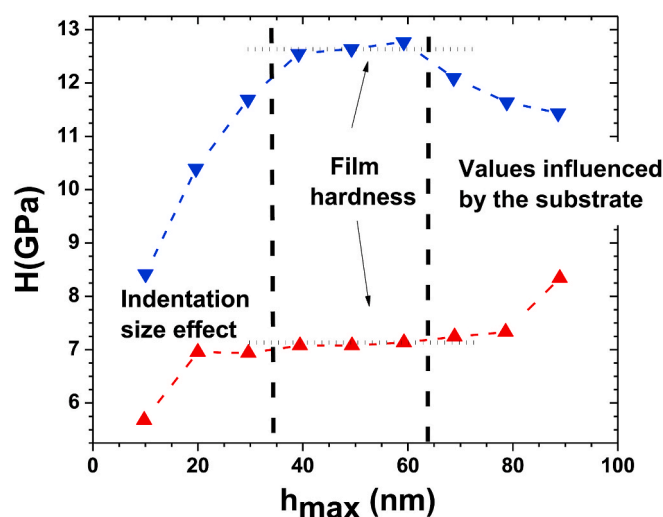


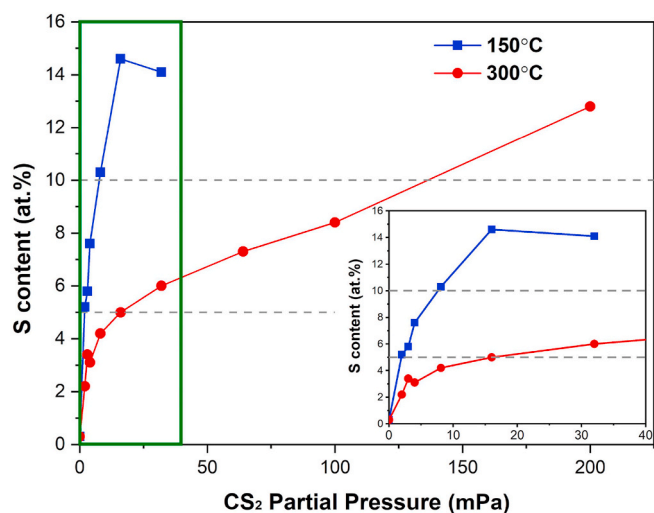
Fig. 1. Hardness versus nanoindentation depth for a hard CS $_x$  sample deposited at: (▼) 150 °C and [S/C] = 5.25% and (▲) 300 °C and [S/C] = 15%. According to ISO 14577 [28], the hardness of the film is the one obtained in the plateau around  $h_{\max} = 50$  nm penetration depth.

Table 1

List of all CS $_x$  film samples together with the corresponding deposition conditions and their composition as per XPS results. The samples containing an “L” in their label were deposited at the lower temperature of 150 °C while those with an “H” in their label were deposited at the higher temperature of 300 °C. The deposition time for the L1 sample was 120 min, while for all other samples it was 180 min.

Sample label	Pressure CS $_2$ (mPa)	Sample order by decreasing C content	Composition by XPS (at.%)			
			C	S (2p)	O	F
L1	0	1	96.1	0.3	3.6	
L2	2.0	2	95.4	1.8	2.8	
L3	3.0	3	92.6	5.2	2.2	
L4	3.0	4	92.5	5.8	1.7	
L5	4.0	5	90.4	7.6	2.0	
L6	8.1	6	86.1	10.3	3.6	
L7	16	8	83.5	14.6	1.9	
L8	16	9	83.3	14.4	2.3	
L9	32	7	84.2	14.1	1.7	
H1	0	1	96.5	0.3	3.2	
H2	2.0	2	95.2	2.2	2.4	0.2
H3	3.0	3	94.6	3.4	1.9	0.1
H4	3.0	5	94.4	2.9	2.7	
H5	4.0	4	94.6	3.1	2.3	
H6	8.0	6	93.7	4.2	2.1	
H7	16	7	93.1	5.0	1.9	
H8	32	8	92.0	6.0	2.0	
H9	64	9	90.9	7.3	1.8	
H10	100	10	89.8	8.4	1.8	
H11	200	11	85.5	12.8	1.7	

that for deposition at 150 °C the S content in the film is more than 5 at.% (5.2 at.%) already at a pCS $_2$  of 2 mPa and close to 15 at.% (14.6 at.%) at a pCS $_2$  of 16 mPa. A further increase of the pCS $_2$  seems to yield no effect on the S content in the films. This observation is interesting as it suggests an upper limit for the S content in CS $_x$  films deposited at 150 °C. This can perhaps be understood from an increased probability for desorption from S-rich surfaces as triggered by the formation of volatile S-rich (or purely S-containing) clusters of 2–5 atoms and relatively high stability thus removing S atoms from the film edge as described from previous theoretical results [22]. From Fig. 2, we also find that the films deposited at 300 °C follow the same general trend as those grown at 150 °C, but the same partial pressures applied at this higher temperature result in lower S contents. The lower S content obtained at 300 °C can be explained



**Fig. 2.** S content of all  $\text{CS}_x$  film samples vs. the corresponding  $\text{CS}_2$  partial pressure during their deposition. The area delimited by the green rectangle corresponding to  $\text{CS}_2$  partial pressures 0–40 Pa is enlarged in the inset. (For interpretation of the references to colour in this figure legend, the reader is referred to the Web version of this article.)

through a competing process where desorption of S, adsorbed on the growing  $\text{CS}_x$  films, is corroborated by higher deposition temperatures. Such observation agrees with our previous detailed findings for  $\text{CP}_x$  films deposited from a compound source at 150 and 450 °C [13], where the higher temperature resulted in lower P content. Since O content in the samples is very low (Table 1), the C content curve as a function of the deposition pressure of  $\text{CS}_2$  is nearly fully complementary to the S content curve depicted in Fig. 2. Thus, the C content is decreasing for both temperatures, but with lower C content in the films deposited at 150 °C as a result of the reciprocally higher S content in these films. The inset in Fig. 2 illustrates the much slower decline of the C content in the  $\text{pCS}_2$  range of 0–32 mPa in films grown at 300 °C compared to those deposited at 150 °C with ~92 at.%, and ~84 at.% at  $\text{pCS}_2 = 32$  mPa, respectively.

Furthermore, the XPS analysis (discussed in detail in the next section) shows an O content of typically ~2 to ~4 at.% and with no influence seen from the applied growth temperature and with the highest O content found in the C reference films. Here we note that no sputter cleaning was performed on these previously air exposed films, which suggests that the O contaminants are adsorbed species on the surface, and thus implies a higher purity in the bulk of all films studied here. Features in the O 1s XPS binding energy ranges of 532.6–532.7 and 531.6–531.7 eV (not shown) suggest that the O-containing species mainly are adsorbed water ( $\text{H}_2\text{O}$ ) and hydroxyl (OH), respectively [25]. The latter is more pronounced at  $\text{CS}_x$  films with high S content, which suggests that OH mainly bonds to S-sites. Hence, from the quantitative analysis, we find that our films are of well-defined compositions and with a low level of contaminants, which is ideal both for fundamental studies of their nature, and for their prospects as protective coatings.

### 3.2. Chemical bonding structure of the $\text{CS}_x$ films

XPS was applied to determine the chemical bonding structure of the  $\text{CS}_x$  films. Chemical analysis of carbon sulfides is, however, a challenge because the electronegativities of C and S are almost identical; according to the Pauling scale they are 2.55 and 2.58, respectively [29]. Because of the small difference in electronegativity the atomic charge of both C and S is almost zero and the chemical shifts between pure C,  $\text{CS}_x$ , and  $\text{CS}_2$ , as well as between pure S,  $\text{CS}_x$ , and  $\text{CS}_2$ , are very small.

Representative C 1s and S 2p XPS spectra of the obtained pure C and  $\text{CS}_x$  films deposited at 150 °C are shown in Fig. 3. The  $\text{CS}_x$  film deposited using, e.g.,  $\text{pCS}_2$  of 8 mPa shows a C 1s peak at 284.6 eV, which can be

compared with the C 1s peak obtained from the pure C that shows a C 1s peak at 284.4 eV. The binding energy of 284.6 eV suggests a carbon-based film of  $\text{sp}^2$  bonding [30] with no inclusion of  $\text{CS}_2$ ; the C 1s binding energy of  $\text{CS}_2$  is 287.2 eV [31]. The corresponding S 2p spectra show the  $2p_{3/2}$  and  $2p_{1/2}$  spin-orbit split components at 163.7 and 164.8 eV, respectively, which is 0.2 eV lower compared to that previously reported for  $\text{CS}_2$  [32]. In addition, there is a relatively broad  $2p_{3/2}$  feature around 161.8 eV, which is assigned to adsorbed S atoms and dimers on the surface of the  $\text{CS}_x$  film [33,34].

Fig. 4 shows that the C 1s and S 2p binding energy positions depend on the S content and that the core level shifts are positive for both C 1s and S 2p. This behavior indicates a charge depletion in the  $\text{CS}_x$  film as the  $\text{pCS}_2$  increases. This is due to the charge transfer from the  $\text{CS}_x$  film towards the adsorbed S atoms and dimers as the amount of the adsorbed species grows with  $\text{pCS}_2$ , see the intensity increase at 161.8 eV in Fig. 3. More important, though, is the observation that the core level shifts are synchronized, which indicates that the S atoms that are represented by the S 2p peaks at 163.7 and 164.8 eV are incorporated in the C  $\text{sp}^2$  bonding network. Since the electronegativity of C and S are nearly the same, the observed shifts might seem unexpected. However, the deposited  $\text{CS}_x$  films are conductive and, thus, have free moving electrons that flow in the graphene-like network. Discontinuities in the network, such as vacancies, incorporated atoms of different sizes, and adsorbed atoms, attract the free moving electrons to screen the “defects” in the graphene-like network [24]. Hence, the adsorbed S atoms and dimers that are adsorbed on the C  $\text{sp}^2$  bonded network with incorporated S will attract charge from the C and S in  $\text{CS}_x$ , not because of difference in electronegativity but because of surface atom screening.

Representative C 1s and S 2p XPS spectra of the obtained pure C and  $\text{CS}_x$  films deposited at 300 °C are shown in Fig. 5. For the  $\text{CS}_x$  films deposited at 300 °C the S content in the films is lower compared to the

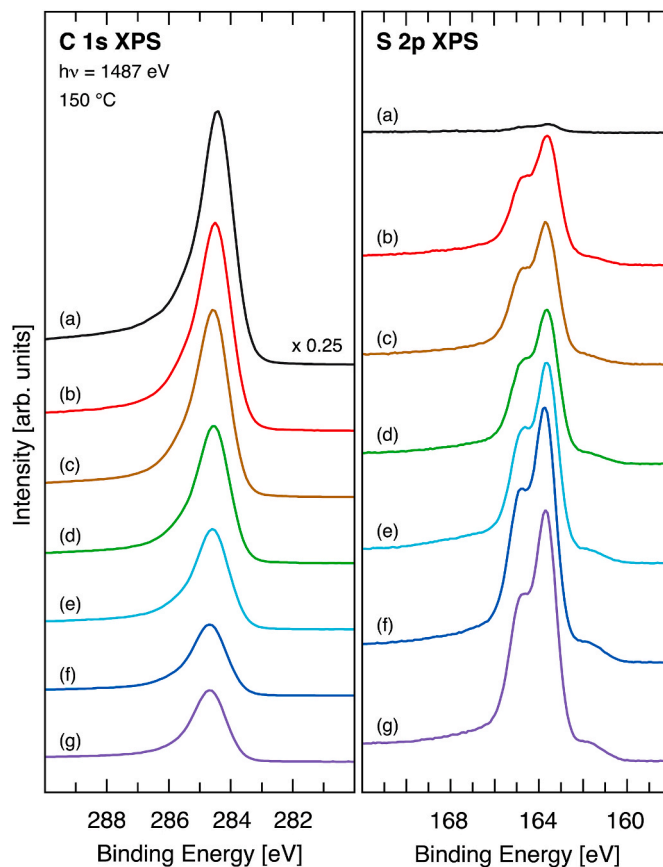


**Fig. 3.** C 1s and S 2p XPS of  $\text{CS}_x$  film deposited at 150 °C. The partial pressures of  $\text{CS}_2$  are (a–g) 0, 2, 3, 4, 8, 16, and 32 mPa.



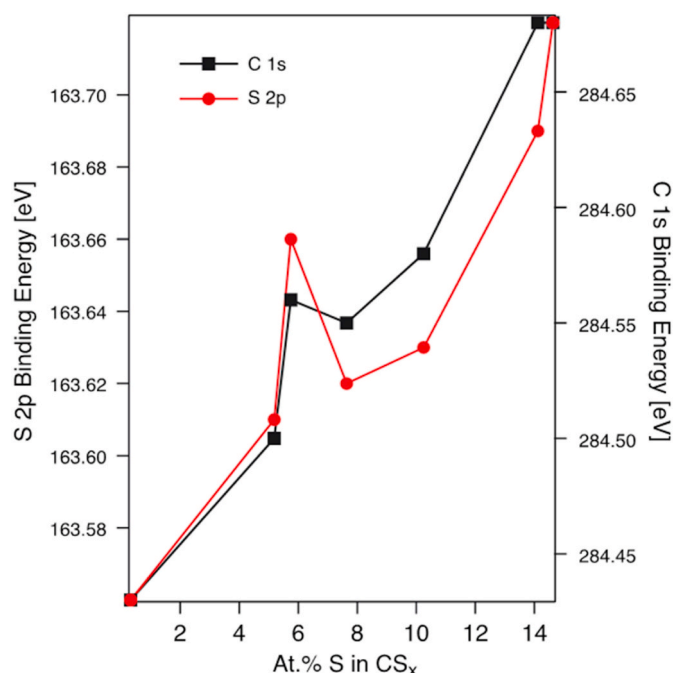


Fig. 4. C 1s and S 2p core level shifts for  $\text{CS}_x$  film deposited at 150 °C with increasing S content.

corresponding  $\text{CS}_x$  films deposited at 150 °C for all selected  $\text{pCS}_2$ . Except from dissimilar reaction yields, the XPS features do not show any significant difference between  $\text{CS}_x$  films deposited at the two temperatures

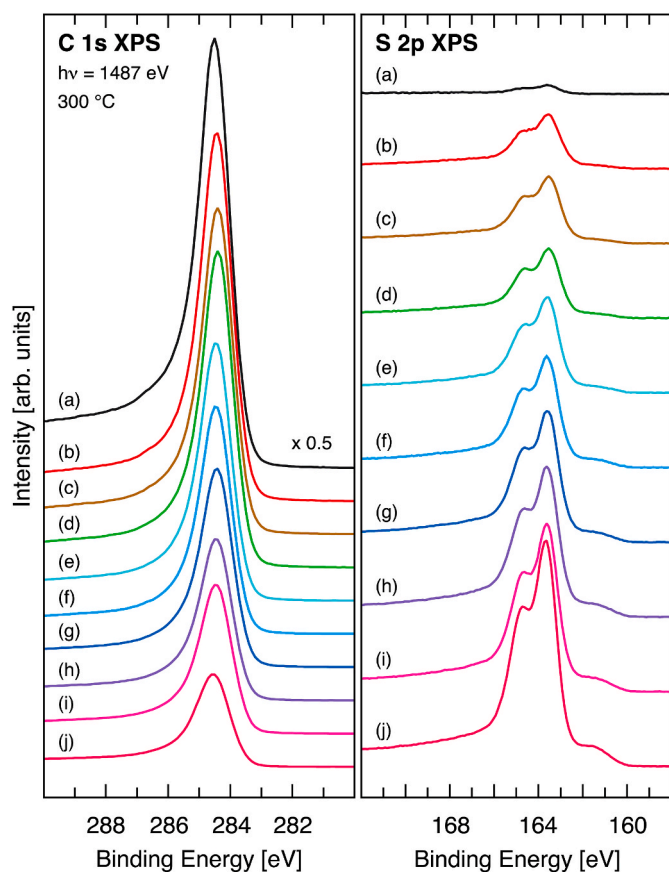


Fig. 5. C 1s and S 2p XPS of  $\text{CS}_x$  film deposited at 300 °C. The partial pressures of  $\text{CS}_2$  are (a–j) 0, 2, 3, 4, 8, 16, 32, 64, 100, and 200 mPa.

150 °C and 300 °C. However, all C 1s and S 2p XPS spectra of the  $\text{CS}_x$  films deposited at 300 °C show a shift of about  $-0.1$  eV compared to the  $\text{CS}_x$  films deposited at 150 °C. Simultaneously, the corresponding O 1s spectra show a shift of about 0.1 eV. This suggests an extra charge transfer from the absorbed oxygen species toward the  $\text{CS}_x$  films deposited at 300 °C, compared to the  $\text{CS}_x$  films deposited at 150 °C, most likely because of a stronger bond to the  $\text{CS}_x$  surface. Hence, the surfaces of the two  $\text{CS}_x$  films are slightly different.

### 3.3. Raman characterization of the $\text{CS}_x$ films

The Raman spectra of  $\text{CS}_x$  films with various S content are shown in Fig. 6(a) and (b), for the series of samples deposited at substrate temperatures of 150 °C and 300 °C, respectively. The S content is denoted for each spectrum and decreases from top to bottom in both panels. As seen from Fig. 6, all the spectra show the characteristic D and G peaks of amorphous carbon. In order to estimate the parameters of these peaks in the different spectra, we have performed fitting of the spectra using two Gaussian line shapes (for D and G), which seem to provide reasonable fits to all spectra (see the Supplementary Information). The fitting enables us to estimate with reasonable accuracy the individual D- and G-peak positions, as well as their linewidths and amplitudes. The D-peak of all Raman spectra is located at  $\sim 1386 \pm 5 \text{ cm}^{-1}$  and does not change markedly its position as the deposition parameters change. The full width at half maximum (FWHM) of the D peak is also roughly the same across the spectra, about  $363 \pm 14 \text{ cm}^{-1}$ .

On the other hand, both the line position of the G-peak and its FWHM show a systematic change with increasing S content. In both series of samples grown at the two different substrate temperatures, 150 °C and 300 °C, the G-peak position exhibits increasing red shift with increasing S content up to  $\sim 7$  at.% S, and, simultaneously, the G-peak FWHM increases (Fig. 7(a)). This observation suggests that the increase of S content is associated with increasing tensile strain in the C-network. In addition, the increasing FWHM of the G-peak with S content suggests increasing disorder in the C-network. At S concentrations above 7 at.%, the G-peak FWHM decreases again and at the highest concentrations (14.1 and 12.8 at.% S for  $T_s = 150$  °C and  $T_s = 300$  °C, respectively) reaches a value close to the value of the corresponding reference sample for each series (0.3 at.% S). The increase of the G-peak FWHM at moderate S concentrations (below  $\sim 7$  at. %) is in line with the expected increased disorder in the C-matrix owing to introduction of S. However, the saturated behaviour of the G-peak position at high S concentrations together with the decreasing G-peak FWHM may indicate a trend for segregation of S from the C-network as predicted by Synthetic Growth Concept modelling of  $\text{CS}_x$  networks [22,23]. Consequently, the incorporation of S in the C-network saturates due to segregation of the excess S at the highest concentrations, hence the disorder and the tensile strain in the latter remain approximately unchanged at S atomic concentrations above  $\sim 7$  at. %. The observed decrease of the G-peak FWHM at S-concentrations beyond  $\sim 7$  at. %, however, may indicate that the tensile stress introduced by the presence of S is more homogeneously distributed at S-concentrations above  $\sim 7$  at. % (when segregation possibly occurs), while the strain and the disorder (indicated also by the D/G ratio to be considered below) remain roughly at the same level as at 7 at. % of S. The mechanism behind this “homogenization” of the strain witnessed by decreasing FWHM at high S at. %, however, is not well understood at present.

Another parameter which can be associated with the properties of the films is the amplitude ratio between the D and G peaks (D/G). Early work [35] tends to associate the value of this ratio with the ratio between the  $\text{sp}^3$  and  $\text{sp}^2$  sites in amorphous carbons (a-C). However, the work of Ferrari and Robertson [36] shows that the D-peak intensity is strictly connected to the presence of six-fold aromatic rings, i.e., hexagons, especially in a-C, quoting just sputtered carbon as an example of a-C. Furthermore, Ref. [36] claims that in a-C the development of D-mode in the Raman spectrum is associated with ordering, exactly

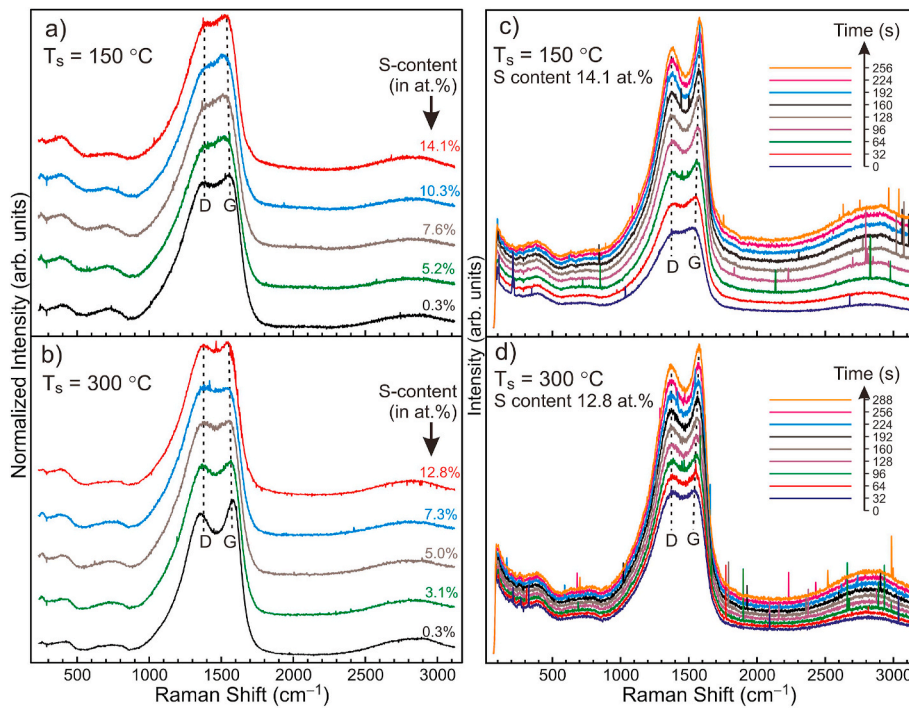


**Fig. 6.** Normalized Raman spectra of  $\text{CS}_x$  films deposited at substrate temperature  $T_s$  of (a) 150 °C, and (b) 300 °C, for various S contents, as denoted for each spectrum. Panels (c) and (d) illustrate the effect of annealing under the action of the exciting laser manifested in changes of the spectrum of the samples with highest S content [14.1 at.% at  $T_s = 150$  °C in (c), and 12.8 at.% at  $T_s = 300$  °C in (d)] with increasing time of illumination. Spikes are visible in the latter two series of spectra, because the spike removal algorithm is disabled in order to acquire a spectrum every 32 s. While the spectra in (a) and (b) are normalized, the spectra in (c) and (d) are simply overlaid without rescaling or vertical shift, thus illustrating the appearance of growing luminescence background and the intensity increase of the D and G peaks with increasing time. The bottom curve in each of the parts (c) and (d) represents the spectrum recorded first after the ignition of the laser, and every subsequent spectrum towards the top of the stack is recorded approximately 32 s later.

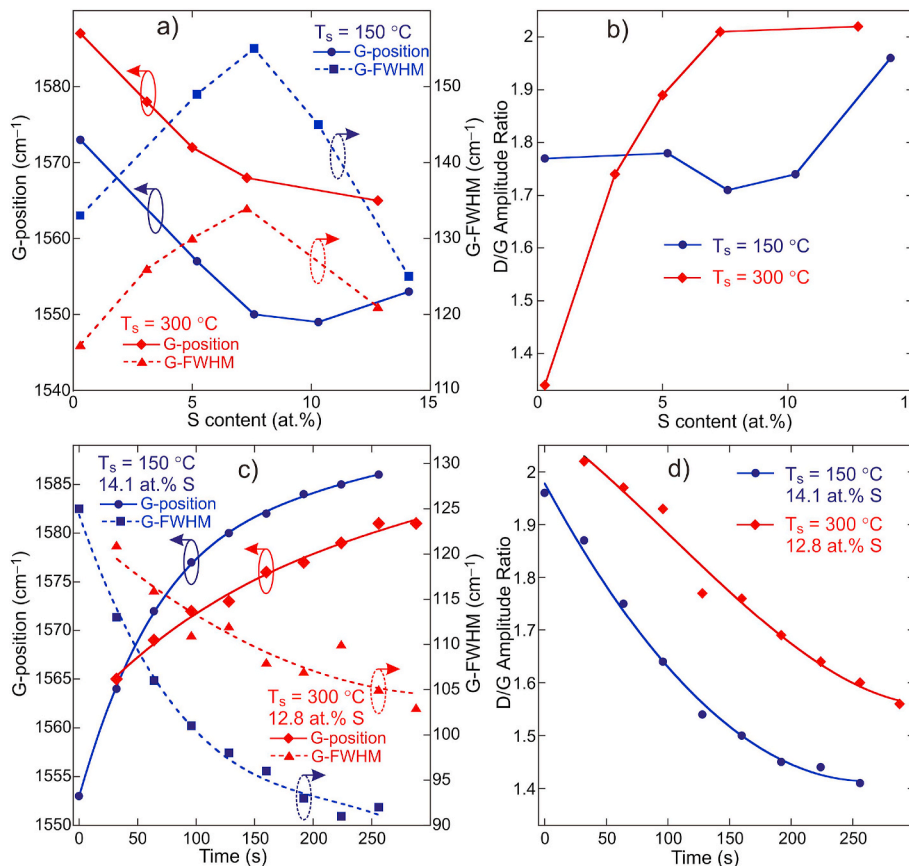


**Fig. 7.** Summary of the G- and D-peak parameters obtained from fitting of the spectra. Variation of (a) the G-peak position and FWHM, and (b) the D/G amplitude ratio with the S content for the two substrate temperatures, as denoted for each set of points. Panels (c) and (d) are related to the subsequent spectra taken on the same spot for the samples with highest S content at the two substrate temperatures and illustrate: (c) variation of the G-peak position and FWHM with time after laser ignition, and (b) variation of the D/G ratio with time under laser annealing. As denoted in all panels, the blue symbols and curves refer to the samples grown at  $T_s = 150$  °C and the red symbols and curves – to the samples grown at  $T_s = 300$  °C. The lines connecting the points (or passing through the sets of points) are guide to the eye. (For interpretation of the references to colour in this figure legend, the reader is referred to the Web version of this article.)

opposite to the case of graphitic carbons studied in Refs. [35]. Two “regimes” for disordered carbon networks are proposed in Ref. [38], a-C regime (e.g., sputtered C), where the intensity ratio  $I(\text{D})/I(\text{G})$  is proportional to  $L_a^2$ , and graphitic carbon regime, in which  $I(\text{D})/I(\text{G})$  is

proportional to  $1/L_a$ . Here  $L_a$  denotes the average graphitic-cluster size. Ref. [36] also admits a broad transition region between the two regimes. Our results for the D/G ratio dependence on the S content for the two deposition temperatures are shown in Fig. 7(b). The D/G ratio increases

substantially with increasing S content for the samples sputtered at 300 °C (between 1.34 and 2.02 for S content between 0.3 and 7.3%), but it remains nearly constant (between 1.71 and 1.78) in the range of S content between 0.3 and 10.3% for the samples grown at 150 °C. The increasing D/G ratio with increasing S content in the series of samples grown at 300 °C is consistent with the theoretically predicted increasing disorder, including incorporation of pentagons and heptagons instead of hexagons, caused by incorporation of S in the C-network [23]. In the series grown at 150 °C there is a trend for increase of D/G at the highest concentration (14.1%), albeit there is no specific trend at lower S concentrations (note that D/G remains quite high compared to the samples grown at 300 °C). Thus, apparently, in our case increasing D/G indicates increasing disorder. This notion is in contrast with the model of [36] predicting *decreasing* disorder with increasing D/G for a-C, possibly because the samples considered here are within the transition region of Ref. [36]. Thus, our notion is based on the experimental results obtained from our set of sputtered samples. The fact that larger D/G indicates larger disorder is reflected also in the initial (reference, at S-content 0.3%) values of D/G at the two temperatures,  $D/G \approx 1.33$  for the reference sample grown at 300 °C, whereas the corresponding value of the sample grown at 150 °C is  $D/G \approx 1.77$ . Indeed, the C-matrix tends to order at higher temperatures, hence, the lower D/G ratio of the film grown at 300 °C must be associated with higher degree of order.

The above consideration is corroborated by the observation of a laser annealing effect in the films with highest S-content in the two series, 14.1% at  $T_s = 150$  °C, and 12.8% at  $T_s = 300$  °C. Despite the low laser-applied power of 0.5 mW, these two films become annealed under the laser excitation. This is indicated by the change of the spectra taken sequentially every ~32 s during ~5 min interval, as illustrated in Fig. 7 (c and d) for  $T_s = 150$  °C and  $T_s = 300$  °C, respectively. We notice that none of the remaining samples with lower S content shows any notable changes in the Raman spectrum with time. Note that the spectra in both panels of Fig. 6(c and d) are overlaid without rescaling and without application of vertical shift to the individual curves. Thus, both series of spectra manifest also increase of the luminescence background with time because of the laser annealing, as well as a very pronounced increase in the Raman intensity. The increasing luminescence background supports the idea that at the highest S content the annealing leads to polymerization of the films, at least in some microscopic volumes within the laser spot on the sample. Furthermore, any annealing is expected to relieve strains present in the sample and, indeed, this is reflected in the large relaxation of the G-peak position towards that of the reference sample, as shown in Fig. 7(c). In addition, the G-peak FWHM decreases with the annealing time, also towards (or even below) the lowest value of  $115 \text{ cm}^{-1}$  observed in the reference sample (0.3 at.% of S at  $T_s = 300$  °C), cf. Fig. 7(c). Notably, the annealing effect is strongest in the sample grown at  $T_s = 150$  °C expressed in larger blue shift of the G-peak position, larger decrease in its FWHM and larger decrease of the D/G ratio compared to the sample at  $T_s = 300$  °C. The latter is plotted as a function of the annealing time in Fig. 7(d) and clearly illustrates that the annealing leads to substantial decrease of the D/G ratio. Thus, again, the decreasing D/G ratio must be associated with increasing order in the C matrix.

Finally, the increase of the Raman signal with annealing time in both samples is most probably associated with decrease of the band gap of the C matrix. Thus, the films become more transparent with annealing, leading to increase of the Raman peaks.

We comment now on the observed dependencies of the G-peak position, the G-peak linewidth and the D/G ratio on the S content in the range 0.3% – approximately 10%. The observed softening of the G mode with increasing S % is well pronounced at both deposition temperatures, as illustrated in the insert of Fig. 7(a). This softening is most likely associated with the anticipated increased curvature evidencing increased tensile strain in  $\text{CS}_x$  sheet fragments composing the C network as referred by theoretical prediction [23]. Simultaneously, with increasing S content, the disorder in the C network increases as

suggested by the increasing FWHM of the G peak; this feature is well pronounced also for both growth temperatures, as long as S contents below ~10% are considered (cf. Fig. 7(a)). Here, we intentionally discard the three points with the highest S content (10.3% and 14.1% at  $T_s = 150$  °C, and 12.8% at  $T_s = 300$  °C). For these highest S contents, the G-FWHM tends to decrease again and the G-peak position saturates (cf. Fig. 7(a)). This behavior may be due to the formation of  $\text{CS}_x$  domains with amorphous structure and short and interlocked graphene-like planes of the film that coexist with areas of the film with predominantly a-C that includes small regions of partial segregation of S, as already discussed above. As mentioned in the Introduction, formation of amorphous C films with close order bonding pattern is expected theoretically for S contents in the range 10–15%. Thus, from the Raman results one may conclude that for S content below ~7% the C matrix is doped with S and its properties gradually change with increasing S content. At S content above ~10%, however, more extended amorphous  $\text{CS}_x$  domains with close order bonding pattern are formed while coexisting with areas where the S atoms tend to segregate allowing the C matrix in these areas to relax to a state close to that without S.

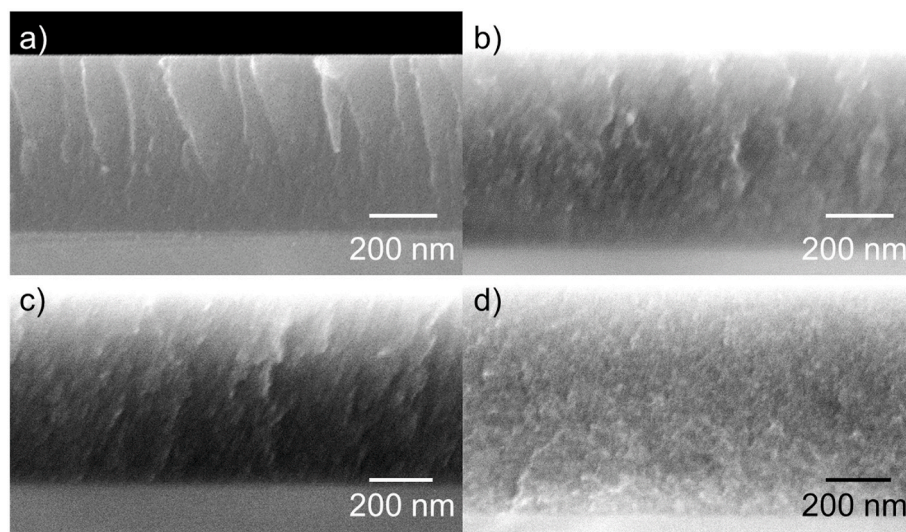
### 3.4. Structural properties of the $\text{CS}_x$ films

Fig. 8 shows SEM images obtained from films deposited at 150 and 300 °C. The image in Fig. 8(a) to which may be attributed a “flake-like” (lamella-like) columnar microstructure is from a film containing 10.3 at.% S ( $p\text{CS}_2 = 8$  mPa during growth) that was deposited at 150 °C. This microstructure is similar to that of a  $\text{CP}_x$  film containing 10 at.% P grown at 300 °C [13]. Increasing the S content in these films up to ~14 at.% ( $p\text{CS}_2 = 32$  mPa during growth) results in a more amorphous structure like that displayed in Fig. 8(d). This shows that the S content affects the film microstructure probably by the S segregation and formation of S clusters, which is also in agreement with the Raman results. These results are also in agreement with the theoretical calculations predicting the formation of amorphous  $\text{CS}_x$  with close order bonding pattern between 10 and 15 at.% S with increasing probability for S segregation at higher S contents [22]. In addition, a higher S content in these films also results an increased film thickness seen from the 565 nm thick film in Fig. 8(a) compared to 660 nm for a film containing 14.1 at.% S, not shown. This can be explained by the higher  $p\text{CS}_2$  applied during growth to give more S and additional evaporated C to the films. The films deposited at 300 °C, Fig. 8(b-d) all show a predominantly amorphous microstructure. The C-reference film in Fig. 8(b) displays broken columns, while adding 4.2 at.% of S ( $p\text{CS}_2 = 8$  mPa during growth) to the film in Fig. 8(c) and 8.4 at.% ( $p\text{CS}_2 = 32$  mPa during growth) in Fig. 8(d) leads to amorphous microstructure. This supports the fact that S affects the microstructure and with potential mechanism seen from an increased desorption of S at this higher temperature. The  $\text{CS}_x$  films deposited at 300 °C follow the same trend with respect to film thickness as those grown at 150 °C. The SEM analysis shows that the S content in the  $\text{CS}_x$  film significantly affects the microstructure for the films, especially those deposited at 150 °C. The influence of the S content on the  $\text{CS}_x$  microstructure is an indication that the S content will be a factor with an impact on their mechanical properties.

### 3.5. Mechanical properties of the $\text{CS}_x$ films

The dependence of the Hardness H on the S concentration for all samples deposited at 150 °C and at 300 °C, respectively, is shown in Fig. 9. Samples deposited at 150 °C are harder (9–15 GPa) than samples deposited at 300 °C (~6.5–9 GPa). For both series of samples deposited at 150 °C and 300 °C, we observe a clear trend for increasing of the film hardness with the growing S content which starts at relatively low S concentrations of ~2 at.%. The maximal hardness of ~13 GPa is achieved for ~5.75 at.% of S (sample deposited at 150 °C). At ~5.75–6 at.% of S, for both series of samples deposited at different temperature, the hardness starts to decrease with the increasing S content, but up to 10 at.





**Fig. 8.** SEM images representing the microstructure of: (a, upper left panel)  $\text{CS}_x$  film containing 10.3 at.% S ( $\text{pCS}_2 = 8$  mPa during growth) deposited at 150 °C; (b, upper right panel) C reference film ( $\text{pCS}_2 = 0$  mPa), 0.32 at.% S deposited at 300 °C; (c, bottom left panel)  $\text{CS}_x$  film containing 4.2 at.% of S ( $\text{pCS}_2 = 8$  mPa during growth), deposited at 300 °C; (d, bottom right panel)  $\text{CS}_x$  film containing 8.4 at.% of S ( $\text{pCS}_2 = 32$  mPa during growth), deposited at 300 °C.

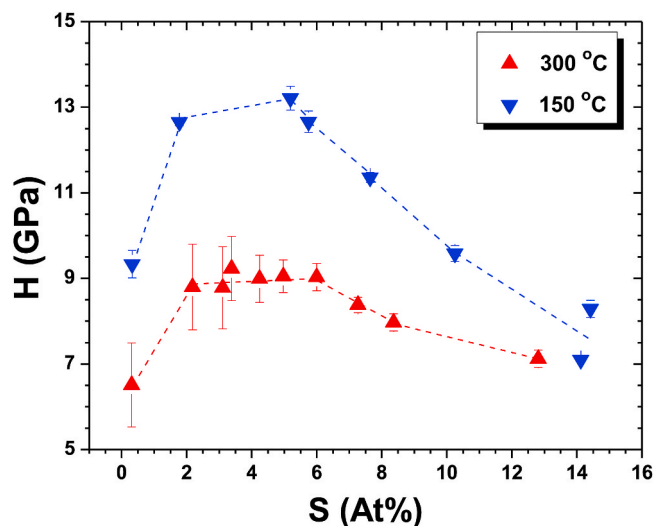


**Fig. 9.** Hardness  $H$  vs  $S$  concentration for samples deposited at 150 and 300 °C. The lines connecting the points (or passing through the sets of points) are simply guide to the eye. Values and error bars for  $H$  were averaged from 12 indents to determine the mean value and standard deviations.

% S (150 °C) and up to ~15 at.% (300 °C) remains higher than that of the reference sample. For samples deposited at both temperatures, samples with 2 and 8 at.% S exhibit high hardness compared to those with none or negligible S contents and those with S content higher than 10 at.%.

There are very few reports on the mechanical properties of  $\text{CS}_x$  films. Although deposited by other methods, adopting different sample systematics, and only reporting the coating hardness, these previous reports highlight an interest in  $\text{CS}_x$  films because of their potentially valuable mechanical properties. Kumari and Subramanyam studied the structural, electrical, and mechanical properties of 1–2  $\mu\text{m}$  thick amorphous C–S composite films deposited by vapor phase pyrolysis of maleic anhydride and sulfur at 900 °C [37]. The Vickers microhardness values ( $H_V$ ) obtained by applying 100 g force (0.98 N) show that the hardness increases with an increase in S concentration. As it has been recently discussed [27], although Vickers indentation values cannot be compared with our Berkovich nanoindentation measurements, the authors of

Ref. [37] correlate the increase of hardness while increasing S concentration with a possible increase in the connectivity of the  $\text{sp}^3$  matrix in the a-C system. Freyman et al. synthesized hydrogenated amorphous carbon films by pulsed dc magnetron sputtering in a mixture of  $\text{Ar}/\text{H}_2/\text{H}_2\text{S}$  [38]. It was observed that film nanoindentation hardness decreases from 13 GPa for pure C films to  $8 \pm 1$  GPa with 5 at.% S doping. They proposed that the decrease in hardness with the increase of S incorporation is most likely due to S interruption of the 3D-bonding network of C atoms. Finally, Hiraide et al. synthesized S-doped amorphous C thin films by plasma CVD using thiophene ( $\text{C}_4\text{H}_4\text{S}$ ) as a starting material [39]. They observed that, when the deposition temperature was increased from 50 to 350 °C, the nanoindentation hardness and the density also increased from 6.5 to 9.6 GPa, and from 1.7 to 1.9  $\text{g}/\text{cm}^3$ , respectively. However, XPS characterization show that, for all deposition temperatures, the concentration ratio S/C kept constant at ~8%. In contrast to our work, the availability of hydrogen-containing precursor species in the experiments conducted by Hiraide et al. may significantly influence the film growth and film bonding leading to softer films especially at lower temperatures. Thus, by choosing  $\text{CS}_2$  for source of S, we achieve higher hardness (up to ~13 GPa as compared to 9.6 GPa) for wider S content and at lower deposition temperatures than in Ref. 39.

Considered in the context of the similar FL and amorphous carbon-based films, the hardness of ~13 GPa achieved in this work for  $\text{CS}_x$  (5.75 at.% S) comes relatively close to the hardness of hardest examples of FL- $\text{CN}_x$  (15.4 GPa, for  $\text{CN}_x$  containing 16 at.% N) [40], while the hardest to date  $\text{CP}_x$  films are significantly harder at ~24 GPa (achieved for  $\text{CP}_x$  films containing 10 at.% P) [40].

The dependence of the reduced elastic modulus  $E_r$  vs. the S concentration for all samples deposited at 150 °C and at 300 °C, respectively, is shown in Fig. 10. Quite remarkably, the reduced elastic modulus vs. the S concentration in the films follows much the same trend as the hardness, namely samples with 2 and 8 at.% S exhibit high reduced elastic modulus  $E_r$ , while the highest value of  $E_r$  is achieved at about 6 at.% of S. Again, samples deposited at 150 °C exhibit significantly higher reduced elastic modulus (~85–125 GPa) than samples deposited at 300 °C (~55–85 GPa).

These finding for the hardness and the reduced elastic modulus can be explained by the gradual change in the C networks, which with increasing S contents, increasingly acquire  $\text{sp}^3$  hybridization, and structural features consisting in short, curved, and interconnected graphene-like sheets, a structure which favors both hardness and elasticity. At about 10% S as well as at higher S contents, this structure



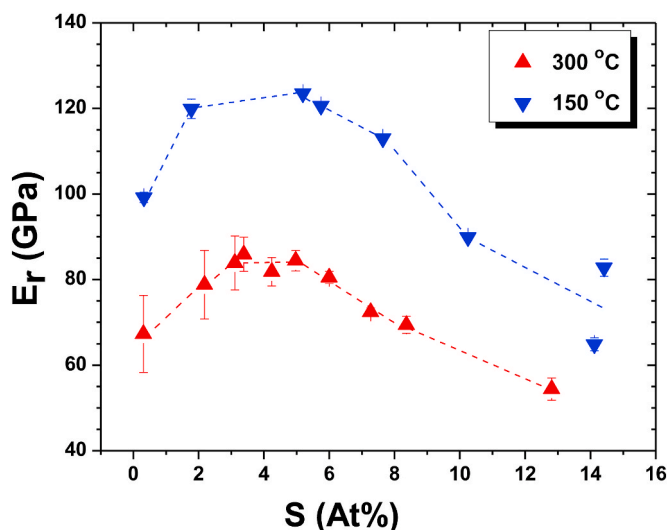


Fig. 10. Reduced elastic modulus  $E_r$  vs S concentration for samples deposited at 150 and 300 °C. The lines connecting the points (or passing through the sets of points) are simply guide to the eye. Values and error bars for  $E_r$  were averaged from 12 indents to determine the mean value and standard deviations.

becomes more and more disordered and strained, perhaps some S segregation is added and becomes significant at S concentrations of ~15 at.%. The S segregation reduces the close order bonding pattern structural features and thus causes decrease in both the hardness and the elasticity of the film. This explanation of the mechanical properties of the  $CS_x$  films are corroborated by the Raman spectra discussed above in Sec. 3.3, and, remarkably well by the theoretical findings in Ref. 23 for well-structured amorphous  $CS_x$  films with close order bonding pattern up to 10 at.% of S, while at higher concentrations of S this network is gradually disrupted, including by domains of S segregation.

Consequently, if the purpose for deposition of  $CS_x$  thin films by using  $CS_2$  as precursor is their application as protective coatings, i.e., putting an emphasis on their hardness and elasticity, the results in this work point out to optimal S content of the films of about 6 at.% and low deposition temperature (150 °C).

#### 4. Conclusions

We deposit  $CS_x$  thin solid films by rDCMS of C target in an Ar plasma, using carbon disulfide ( $CS_2$ ) as S precursor at two different temperatures of 150 °C and 300 °C. XPS analyses show that S content of the films varies between 0.3 and 14.6 at.% and suggests that O contaminants are absorbed species on the surface. The XPS results indicate that most S atoms are incorporated in a predominantly  $sp^2$ -bonded C network and only minor amount is present in the samples as adsorbed S atoms and dimers. The qualitative picture of the microstructure of the films obtained by SEM imaging varies from resembling lamella-like to more amorphous structure at higher S content and is similar to the microstructure of  $CP_x$  films with analogous P content. The microstructure of the films as well as the results of their Raman characterization and the nanomechanical testing results all point out that with the increasing S content some  $sp^3$  bonding is admixed in the predominantly  $sp^2$  bonded  $CS_x$  network, leading to a characteristic close order bonding pattern featuring amorphous structure with short and interlocked graphene planes for S contents between 2% and 8%. At higher S content, effects of S segregation lead to disruption of this structure and decreased hardness and elasticity of the  $CS_x$  films. These results agree remarkably well with previous theoretical findings obtained by modeling the  $CS_x$  compound by the *ab-initio* Synthetic Growth Concept that predict well-structured close order bonding pattern amorphous  $CS_x$  films up to about 10–15% of S as well as at higher S content increasingly significant S segregation

incorporated in the  $CS_x$  network.

In addition, the films deposited at the lower temperature of 150 °C exhibit higher hardness (9–13 GPa) than samples deposited at 300 °C (~6.5–9 GPa), and higher reduced elastic modulus (~85–125 GPa) than samples deposited at 300 °C (~55–85 GPa). Thus, our results indicate that best candidates for hard and elastic  $CS_x$  thin solid films deposited by using  $CS_2$  as precursor would be  $CS_x$  films deposited at low temperature of ~150 °C and with an S content in the region of 6 at.%. The combination of hardness and elastic modulus obtained here for  $CS_x$  thin solid films is suggestive for potential applications as protective coatings, e.g., for steel rolling bearings. The hardness of coatings used nowadays to coat rollers and balls is usually in the range 10–14 GPa. Indeed, higher hardness cannot be used because any higher hardness would increase the wear of the steel counter-face.

#### Declaration of competing interest

The authors declare that they have no known competing financial interests or personal relationships that could have appeared to influence the work reported in this paper.

#### Acknowledgements

HH, JR, and EB acknowledge the Swedish Government Strategic Research Area in Materials Science on Advanced Functional Materials at Linköping University (Faculty Grant SFO-Mat-LiU 2009–00971) for financial support. GKG acknowledges the support by the Swedish Research Council (VR) through FLAG-ERA JTC 2015 project GRIFONE (VR 2015-06816) and VR 2017-04071 as well as Åforsk grant 18–266. IGI acknowledges support from VR via project VR 2016-05362. The National Supercomputer Center (NSC) at Linköping University is acknowledged for providing high performance computing resources. The Knut and Alice Wallenberg (KAW) Foundation supported our thin film and electron microscopy laboratories, and provided funding for a Fellowship Grant (JR) and Project funding (KAW 2015.0043).

#### Appendix A. Supplementary data

Supplementary data to this article can be found online at <https://doi.org/10.1016/j.vacuum.2020.109775>.

#### References

- [1] A.Y. Liu, M.L. Cohen, Structural properties and electronic structure of low-compressibility materials:  $\beta$ - $Si_3N_4$  and hypothetical  $\beta$ - $C_3N_4$ , *Phys. Rev. B* 41 (1990) 10727.
- [2] L. Hultman, J. Neidhardt, N. Hellgren, H. Sjöström, J.-E. Sundgren, Fullerene-like carbon nitride: a resilient coating material, *MRS Bull.* 28 (2003) 194.
- [3] H. Sjöström, S. Stafström, M. Boman, J.-E. Sundgren, Superhard and elastic carbon nitride thin films having fullerenelike microstructure, *Phys. Rev. Lett.* 75 (1995) 1336.
- [4] J. Neidhardt, L. Hultman, E. Broitman, T.W. Scharf, I.L. Singer, Structural, mechanical and tribological behavior of fullerene-like and amorphous carbon nitride coatings, *Diam. Relat. Mater.* 13 (2004) 1882.
- [5] S. Schmidt, G. Greczynski, C. Goyenola, G.K. Gueorguiev, Zs Czigány, J. Jensen, I. G. Ivanov, L. Hultman,  $CF_x$  thin solid films deposited by high power impulse magnetron sputtering: synthesis and characterization, *Surf. Coating. Technol.* 206 (2011) 646.
- [6] S. Schmidt, C. Goyenola, G.K. Gueorguiev, J. Jensen, G. Greczynski, I.G. Ivanov, Zs Czigány, L. Hultman, Reactive high-power impulse magnetron sputtering of  $CF_x$  thin films in mixed Ar/ $CF_4$  and Ar/ $C_4F_8$  discharges, *Thin Solid Films* 542 (2013) 21.
- [7] G.K. Gueorguiev, C. Goyenola, S. Schmidt, L. Hultman,  $CF_x$ : a first-principles study of structural patterns arising during synthetic growth, *Chem. Phys. Lett.* 516 (2011) 62.
- [8] C. Goyenola, S. Stafström, S. Schmidt, L. Hultman, G.K. Gueorguiev, Carbon fluoride,  $CF_x$ : structural diversity as predicted by first principles, *J. Phys. Chem. C* 118 (2014) 6514.
- [9] G. Dearnaley, J.H. Arps, Biomedical applications of diamond-like carbon (DLC) coatings: a review, *Surf. Coating. Technol.* 200 (2005) 2518.
- [10] A. Bendavid, P.J. Martin, L. Randeniya, M.S. Amin, R. Rohanizadeh, The properties of fluorine-containing diamond-like carbon films prepared by pulsed DC plasma-activated chemical vapour deposition, *Diam. Relat. Mater.* 19 (2010) 1466.

- [11] S. Peponas, M. Guedda, M. Benlahsen, On the post-contamination effect on the delamination of sputtered amorphous carbon nitride films, *Solid State Commun.* 146 (2008) 78.
- [12] S. Peponas, M. Benlahsen, M. Guedda, On the delamination dynamic of sputtered amorphous carbon nitride films, *J. Appl. Phys.* 106 (2009), 013525.
- [13] A. Furlan, G.K. Gueorguiev, Zs Czigány, V. Darakchieva, S. Braun, M.R. Corriea, H. Högberg, L. Hultman, Structure and properties of phosphorus-carbide thin solid films, *Thin Solid Films* 548 (2013) 247.
- [14] S. Kundoo, P. Saha, K.K. Chattopadhyay, Electron field emission from nitrogen and sulfur-doped diamond-like carbon films deposited by simple electrochemical route, *Mater. Lett.* 58 (2004) 3920.
- [15] R. Ricardo da Silva, J.H.S. Torres, Y. Kopelevich, Indications of superconductivity at 35 K in graphite-sulfur composites, *Phys. Rev. Lett.* 87 (2001) 147001.
- [16] I. Felner, Y. Kopelevich, Magnetization measurement of a possible high-temperature superconducting state in amorphous carbon doped with sulfur, *Phys. Rev. B* 79 (2009) 233409.
- [17] M. Karuppannan, Y. Kim, Y.-E. Sung, O.J. Kwon, Nitrogen and sulfur co-doped graphene-like carbon sheets derived from coir pith bio-waste for symmetric supercapacitor applications, *J. Appl. Electrochem.* 49 (2019) 57–66.
- [18] Y. Zhou, R. Ma, S.L. Candelaria, J. Wang, Q. Liu, E. Uchaker, P. Li, Y. Chen, G. Cao, Phosphorus/sulfur Co-doped porous carbon with enhanced specific capacitance for supercapacitor and improved catalytic activity for oxygen reduction reaction, *J. Power Sources* 314 (2016) 39–48.
- [19] C.-C. Lai, C. Goyenola, E. Broitman, L.-Å. Näslund, H. Högberg, L. Hultman, G. K. Gueorguiev, J. Rosen, Synthesis and properties of  $\text{CS}_x\text{F}_y$  thin films deposited by reactive magnetron sputtering in an  $\text{Ar}/\text{SF}_6$  discharge, *J. Phys. Condens. Matter* 29 (2017) 195701.
- [20] G.K. Gueorguiev, J. Neidhardt, S. Stafström, L. Hultman, First-principles calculations on the role of CN precursors for the formation of fullerene-like carbon nitride, *Chem. Phys. Lett.* 401 (2005) 288.
- [21] G.K. Gueorguiev, A. Furlan, H. Högberg, S. Stafström, L. Hultman, First-principles calculations on the structural evolution of solid fullerene-like  $\text{CP}_x$ , *Chem. Phys. Lett.* 426 (2006) 374.
- [22] C. Goyenola, G.K. Gueorguiev, S. Stafström, L. Hultman, Fullerene-like  $\text{CS}_x$ : a first-principles study on synthetic growth, *Chem. Phys. Lett.* 506 (2011) 86.
- [23] C. Goyenola, S. Stafström, L. Hultman, G.K. Gueorguiev, Structural patterns arising during synthetic growth of fullerene-like sulfocarbide, *J. Phys. Chem. C* 116 (2012) 21124.
- [24] S. Hüfner, *Photoelectron Spectroscopy: Principles and Applications*, third ed., Springer-Verlag, Berlin, Germany, 2010.
- [25] J.F. Moulder, W.F. Stickle, P.E. Sobol, K.D. Bomben, *Handbook of X-Ray Photoelectron Spectroscopy*, Perkin-Elmer Corporation, Eden Prairie, USA, 1992.
- [26] W.C. Oliver, G.M. Pharr, An improved technique for determining hardness and elastic modulus using load and displacement sensing indentation experiments, *J. Mater. Res.* 7 (1992) 1564.
- [27] E. Broitman, Indentation hardness measurements at macro-, micro-, and nanoscale: a critical overview, *Tribol. Lett.* 65 (2017) 23.
- [28] ISO 14577-4, *Metallic Materials - Instrumented Indentation Test for Hardness and Materials Parameters — Part 4: Test Method for Metallic and Non-metallic Coatings*, International Organization for Standardization, Geneva, 2016.
- [29] W.W. Porterfield, *Inorganic Chemistry: A Unified Approach*, Academic Press, San Diego, 1993.
- [30] M.D. Tucker, Zs Czigány, E. Broitman, L.-Å. Näslund, L. Hultman, J. Rosen, Filtered pulsed cathodic arc deposition of fullerene-like carbon and carbon nitride films, *J. Appl. Phys.* 115 (2014) 144312.
- [31] U. Gelius, P.F. Hedén, J. Hedman, B.J. Lindberg, R. Manne, R. Nordberg, C. Nordling, K. Siegbahn, Molecular spectroscopy by means of ESCA: III. Carbon compounds, *Phys. Scripta* 2 (1970) 70.
- [32] B.J. Lindberg, K. Hamrin, G. Johansson, U. Gelius, A. Fahlman, C. Nordling, K. Siegbahn, Molecular Spectroscopy by Means of ESCA II. Sulfur compounds. Correlation of electron binding energy with structure, *Phys. Scripta* 1 (1970) 286.
- [33] J. Hrbek, S.Y. Li, J.A. Rodriguez, D.G. van Campen, H.H. Huang, G.-Q. Xu, Synthesis of sulfur films from  $\text{S}_2$  gas: spectroscopic evidence for the formation of  $\text{S}_n$  species, *Chem. Phys. Lett.* 267 (1997) 65.
- [34] Y. Jiang, X. Liang, S. Ren, C.-L. Chen, L.-J. Fan, Y.-W. Yang, J.-M. Tang, D.-A. Luh, The growth of sulfur adlayers on  $\text{Au}(100)$ , *J. Chem. Phys.* 142 (2015), 064708.
- [35] F. Tuinstra, J.L. Koenig, Raman spectrum of graphite, *J. Chem. Phys.* 53 (1970) 1126.
- [36] A.C. Ferrari, J. Robertson, Interpretation of Raman spectra of disordered and amorphous carbon, *Phys. Rev. B* 61 (2000) 14095.
- [37] L. Kumari, S.V. Subramanyam, Structural and electrical properties of amorphous carbon-sulfur composite films, *Bull. Mater. Sci.* 27 (2004) 289–294.
- [38] C.A. Freyman, Y. Chen, Y.-W. Chung, Synthesis of carbon films with ultra-low friction in dry and humid air, *Surf. Coating. Technol.* 201 (2006) 164–167.
- [39] T. Hiraide, A. Ono, T. Fusegi, N. Takezawa, S. Kuroda, M. Yoshimoto, H. Yamada, Synthesis of sulfur-doped amorphous carbon thin films by plasma CVD using thiophene as a starting material, *J. Ceram. Soc. Jpn.* 111 (2003) 133–136.
- [40] A. Furlan, G.K. Gueorguiev, Zs Czigány, H. Högberg, S. Braun, S. Stafström, L. Hultman, Synthesis of phosphorus-carbide thin films by magnetron sputtering, *phys. Stat. Sol. (RRL)* 2 (2008) 191–193.